Check for updates

OPEN

Intra-striatal AAV2.retro administration leads to extensive retrograde transport in the rhesus macaque brain: implications for disease modeling and therapeutic development

Alison R. Weiss[1], William A. Liguore[1], Jacqueline S. Domire[1], Dana Button[1] & Jodi L. McBride[1,2,3] ✉

Recently, AAV2.retro, a new capsid variant capable of efficient retrograde transport in brain, was generated in mice using a directed evolution approach. However, it remains unclear to what degree transport will be recapitulated in the substantially larger and more complex nonhuman primate (NHP) brain. Here, we compared the biodistribution of AAV2.retro with its parent serotype, AAV2, in adult macaques following delivery into the caudate and putamen, brain regions which comprise the striatum. While AAV2 transduction was primarily limited to the injected brain regions, AAV2.retro transduced cells in the striatum and in dozens of cortical and subcortical regions with known striatal afferents. We then evaluated the capability of AAV2.retro to deliver disease-related gene cargo to biologically-relevant NHP brain circuits by packaging a fragment of human mutant *HTT*, the causative gene mutation in Huntington's disease. Following intra-striatal delivery, pathological mHTT-positive protein aggregates were distributed widely among cognitive, motor, and limbic cortico-basal ganglia circuits. Together, these studies demonstrate strong retrograde transport of AAV2.retro in NHP brain, highlight its utility in developing novel NHP models of brain disease and suggest its potential for querying circuit function and delivering therapeutic genes in the brain, particularly where treating dysfunctional circuits, versus single brain regions, is warranted.

Adeno-associated viruses (AAVs) are small, non-enveloped viruses capable of packaging single-stranded DNA genomes up to ~5 kb in length[1,2]. Originally discovered in 1965[3], AAVs have become attractive agents for safely and effectively delivering gene cargo to a range of biological tissues (e.g. liver, muscle, retina, brain, kidney) in a wide variety of species (e.g. mouse, rat, cat, dog, pig, rabbit, horse, non-human primate, human)[1]. A number of AAV serotypes (e.g. AAV1-9, rh10, DJ, DJ/8) have been identified to date, as well as hundreds of naturally occurring capsid variants of each of these "parent" serotypes[4,5]. Differences between these AAVs are reflected in unique capsid structures, receptor specificity and tissue tropism[6]. For example, AAV6 and AAV8 transduce liver and skeletal muscle with high efficiency[4,7–9], whereas AAV1, AAV2, AAV5 and AAV9 have been shown to transduce several types of cells in the central nervous system (CNS) including neurons, astrocytes, and photoreceptors[2,10–13].

Over the past decade, AAV-based gene therapies have begun to establish a track record of safety and success in human studies. For example, Luxturna (AAV2-RPE65) received Food and Drug Administration (FDA) approval in 2017 for the treatment of inherited retinal disease[14,15] and Zolgensma (AAV9-SMN1) was FDA-approved in May of 2019 to treat spinal muscular atrophy type 1[16]. Additionally, there are ongoing early-stage clinical trials (recruitment and active phases) evaluating AAV-based gene therapies for neurological indications

[1]Division of Neuroscience, Oregon National Primate Research Center, Beaverton, USA. [2]Department of Behavioral Neuroscience, Oregon Health and Science University, Portland, USA. [3]Department of Neurology, Oregon Health and Science University, Portland, USA. ✉e-mail: mcbridej@ohsu.edu

including, but not limited to, the treatment of Parkinson's (AAV2-AADC and AAV2-GDNF), Huntington's (AAV5-miHTT), Batten (AAV2-CUhCLN2, AAVrh10-CUhCLN2 AAV9-CLN3, AAV9-CLN6) and Alzheimer's (AAVrh10-hAPOE2) diseases (www.clinicaltrials.gov). For most of these disorders, disease-specific pathology has been identified in multiple brain regions and so targeting AAV-mediated gene therapeutics to relevant circuits, versus single brain regions, would likely lead to a better therapeutic outcome for affected patients.

In addition to the immense therapeutic potential of AAVs for delivering disease-modifying constructs to the CNS, AAVs also have wide-ranging utility for neuroscience research, from querying brain functions to creating animal models of disease. For example, several groups have downregulated or overexpressed genes in brain regions such as the hippocampus or prefrontal cortex to assess the impact on cognition, circuit dynamics, and synaptic plasticity[17–19]. More recently, AAVs have been used to deliver channel rhodopsins, or designer receptors, to localized brain regions, enabling researchers to stimulate/inhibit specific populations of neurons with optical signals (i.e. optogenetics[20]), or drugs (i.e. chemogenetics[21]). AAVs have also been used to create animal models of CNS disorders by delivering pathogenic constructs to brain regions of interest, such as the overexpression of α-synuclein in the striatum that results in progressive neurodegeneration and motor phenotypes characteristic of Parkinson's disease (PD)[22–24], or of expanded glutamine-encoding CAG repeats to create a striatal degeneration model of Huntington's disease (HD)[22,25,26], or of amyloid beta to reproduce features of Alzheimer's disease (AD)[27,28].

Despite these recent successes, intra-parenchymal applications of AAVs in the CNS remain largely confined to the injected tissue region, or sub-region, because of restricted spread and limited capacity for anterograde and/or retrograde transport. One approach that has been used to improve biodistribution of AAV constructs in the CNS is convection-enhanced delivery (CED), a technique that uses pressure-gradients to spread AAVs greater distances through brain tissue than simple diffusion alone[29–31]. Although this represents an improvement over conventional intraparenchymal infusion techniques, multiple injections are still needed to cover large brain regions or multiple structures. As such, the development of methods capable of distributing AAVs throughout multiple brain regions and biologically relevant circuits offers significant advantages both experimentally and clinically. One way to achieve this is with an AAV capsid capable of strong synaptic transport.

Recently, Tervo and colleagues generated a new AAV2 capsid variant capable of retrograde transport, named AAV2.retro, using an *in vivo* directed evolution approach in mice[32]. Mixed libraries of AAV *cap* variants were injected into discrete regions of the mouse CNS and variants were selected if they efficiently transported to neuronal cell bodies sending long-range projections to the site of AAV injection[32]. Since its creation, AAV2.retro has been used in mouse and rat models to target a multitude of CNS pathways including the amygdala via the ventral medial hypothalamus[33], the thalamus via the anterior cingulate cortex[34], the claustrum via the prefrontal cortex[35], and more[36–38]. Taken together, these studies demonstrate that AAV2.retro is a powerful molecular tool capable of robust retrograde transport enabling the manipulation of neuronal pathways and circuits. However, it is unknown to what degree these features can be recapitulated in the larger and more complex primate brain. Therefore, we assessed the retrograde functionality of AAV2.retro in the nonhuman primate (NHP) brain by characterizing the biodistribution following stereotaxic injection of AAV2.retro expressing enhanced green fluorescent protein (AAV2.retro-eGFP) into the caudate and putamen of rhesus macaques, and comparing this to the biodistribution of its parent serotype, AAV2, injected into the same regions.

The ability to efficiently distribute AAV constructs throughout biologically relevant circuits in the brain offers significant advantages for the development of novel NHP models of neurological disease. Ongoing efforts in our laboratory are focused on creating an AAV-mediated model of HD via delivery of the disease-causing gene, mutant *HTT* (m*HTT*), into the caudate and putamen of adult rhesus macaques. Although it has been well established that the caudate and putamen are severely impacted in HD[39], more recent studies have revealed that an extended network of structures throughout the cortex and basal ganglia are also affected[40,41]. Therefore, in order to refine our AAV-mediated NHP model to more closely mirror the widespread neuropathology documented in human HD patients, we further probed the capability of AAV2.retro to distribute a pathogenic fragment of mutant huntingtin protein (mHTT) throughout the rhesus macaque cortico-basal ganglia network.

Results

Extensive retrograde transport in the rhesus macaque brain following MRI-guided intra-striatal delivery of AAV2.retro-eGFP.

In order to investigate the retrograde transport capability of AAV2.retro in primate brain, naïve adult rhesus macaques were injected with AAV2.retro-eGFP bilaterally into the head of the caudate nucleus (80 μl at one injection site) and the putamen (150 μl over 2 injection sites spread apart by 4 mm). eGFP expression was driven from the human cytomegalovirus (CMV) promoter. The vector cartoon and surgical coordinates are illustrated in Fig. 1a and Table 1 summarizes each surgical case, including animal age, AAV construct, promoter, injectate titer/volume and post-surgical time to necropsy. Serum samples from all animals were tested for anti-AAV2 neutralizing antibodies prior to surgery, and animals were selected only if they had less than 50% inhibition of transduction when serum was diluted to 1:20. There were no adverse surgical events and all animals recovered fully post-infusion. Following a 4-week post-surgical interval, animals were euthanized, brains were collected and the biodistribution of AAV2.retro was visualized via immunohistochemical staining for eGFP in coronal tissue sections throughout the rostral to caudal extent of the brain. We observed dense eGFP positive (eGFP+) staining in the injected regions of the caudate (Fig. 1b) and putamen (Fig. 1c), with the spread partially filling each structure and the highest amount of transduction surrounding each site of injection. In the injected regions, the morphology of eGFP+ cells suggested that the majority of cells transduced were neurons, although transduced glia were noted as well but to a far lesser degree.

In addition to the caudate and putamen, AAV2.retro injection resulted in widespread vector transport and eGFP expression in a total of sixteen cortical areas and eleven subcortical structures. Anatomical boundaries were defined using the rhesus macaque brain atlas developed by Saleem & Logothetis[42]. Table 2 provides a
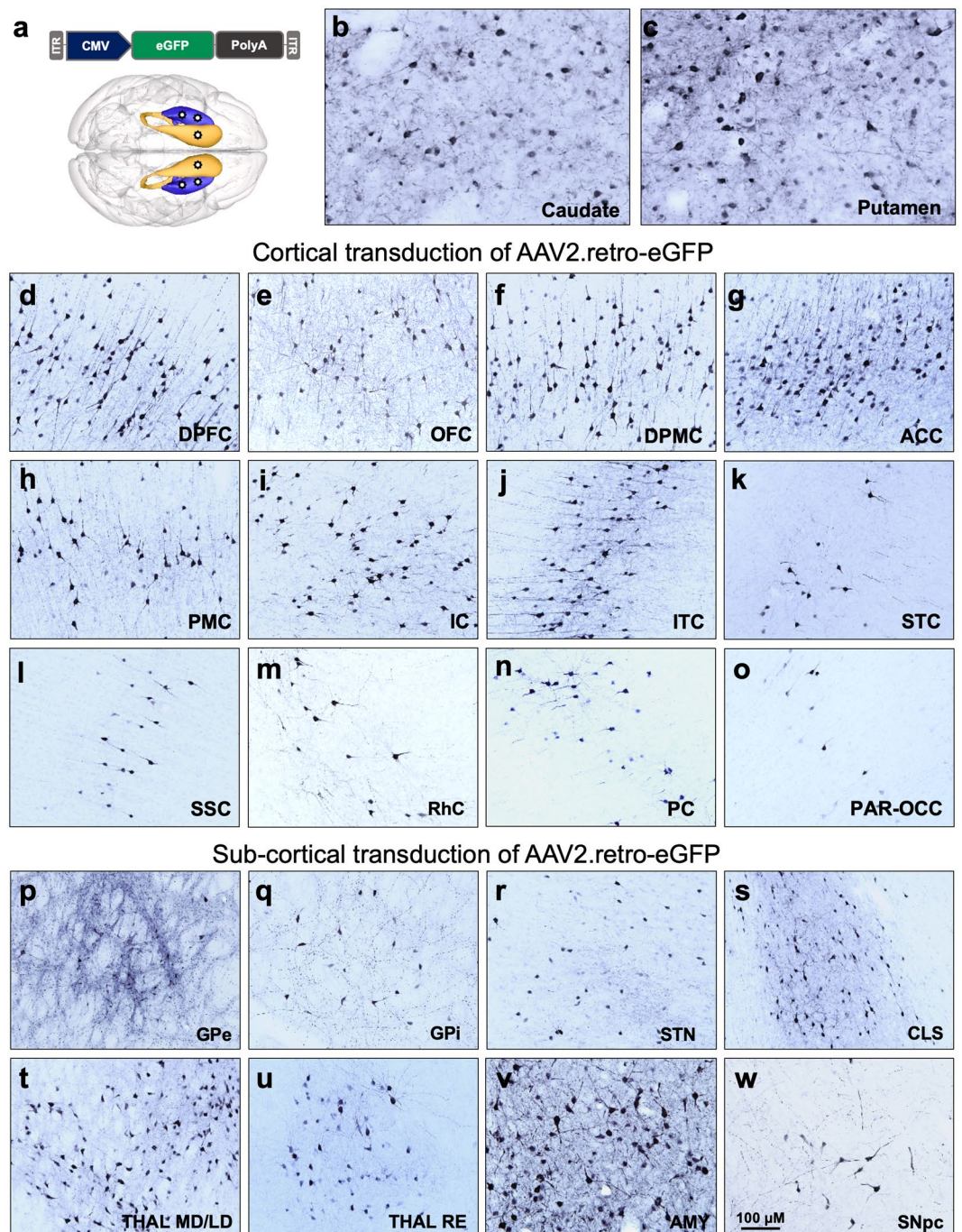
Figure 1. Biodistribution of AAV2.retro-eGFP following intra-striatal injection in adult rhesus macaques. (**a**) Illustrations of the AAV2.retro-eGFP vector construct and injection coordinates into the head of the caudate nucleus and the putamen. Robust eGFP expression in regions directly adjacent to injection sites of the caudate (**b**) and putamen (**c**). Following retrograde transport, additional eGFP expression was found in numerous cortical (**d–o**) regions and subcortical (**p–w**) structures. Abbreviations: AAV (adeno-associated virus), ACC (anterior cingulate cortex), AMY (amygdala), CLS (claustrum), CMV (cytomegalovirus), DPFC (dorsal prefrontal cortex), DPMC (dorsal premotor cortex), eGFP (enhanced green fluorescent protein), GPe (globus pallidus, external segment), GPi (globus pallidus, internal segment), IC (insular cortex), ITC (inferior temporal cortex), ITR (inverted terminal repeat), OFC (orbitofrontal cortex), PAR-OCC (parieto-occipital cortex), PC (parietal cortex), PMC (premotor cortex), PolyA (polyadenylation), RhC (rhinal cortex), SNpc (substantia nigra pars compacta), SSC (somatosensory cortex), STC (superior temporal cortex), STN (subthalamic nucleus), THAL MD/LD (medial dorsal and lateral dorsal thalamic nuclei), THAL RE (reuniens thalamic nuclei). Scale bar in w = 100 microns. Brain graphic in 1a was made using the 3d Brain Composer feature on the Scalable Brain Atlas website (https://scalablebrainatlas.incf.org/composer/?template=CBCetal15).

Animal Number	Animal age at injection	Recombinant AAV Construct	Vector Titer (vg/ml)	Viral Promoter	Caudate Inj. volume/ Hemisphere (μl)	Putamen Inj. volume/ Hemisphere (μl)	Post-surgical interval to necropsy (weeks)
1	9 years	AAV2.retro-eGFP	1×10^{12}	CMV	80	150	4
2	12 years	AAV2.retro-eGFP	1×10^{12}	CMV	80	150	4
3	12 years	AAV2-eGFP	1×10^{12}	CMV	80	150	4
4	16 years	AAV2-eGFP	1×10^{12}	CMV	80	150	4
5	9 years	AAV2.retro-HTT85Q	1×10^{12}	CAG	120	180	10
6	7 years	AAV2.retro-HTT85Q	1×10^{12}	CAG	120	180	10

Table 1. Summary of study participants and surgical cases. AAV- adeno-associated virus, vg- vector genomes, ml- milliliter, μl- microliter, eGFP- enhanced green fluorescent protein, HTT85Q- mutant huntingtin protein bearing 85 CAG repeats, CMV- cytomegalovirus, CAG- chicken beta-actin promotor with a CMV enhancer element.

High	Medium	Low	None
Dorsal prefrontal cortex	Somatosensory cortex	Parietal cortex	Occipital cortex
Ventral prefrontal cortex	Superior temporal cortex	Parieto-occipital cortex	Cerebellum
Orbitofrontal cortex	Inferior temporal cortex	Thalamus (VA/VL)	Substantia nigra, pars reticulata
Dorsal premotor cortex	Rhinal cortex	Thalamus (LP/VPL)	
Ventral premotor cortex	Subthalamic nucleus	Hippocampus	
Anterior cingulate cortex	Globus Pallidus, int. segment		
Pre-supplemental motor cortex	Globus Pallidus, ext. segment		
Supplemental motor cortex	Substantia nigra, pars compacta		
Primary motor cortex	Claustrum		
Insular Cortex	Thalamus (RE)		
Thalamus (MD/LD)			
Amygdala (BLN)			

Table 2. Relative levels of extra-striatal eGFP transgene expression in the rhesus macaque brain following intra-caudate and intra-putamen injection of AAV2.retro-eGFP. Brain regions were qualitatively ranked relative to one another, considering cell number and density, and placed into categories of high, medium, low and minimal/none. All regions listed here had less expression compared to the injected regions of the caudate and putamen. MD- medial dorsal, LD- lateral dorsal, RE- nucleus reuniens, BLN- basolateral nucleus, int.- internal, ext.- external, VA- ventral anterior, VL- ventral lateral, LP- lateral posterior, VPL- ventral posterolateral.

comprehensive list of each of the observed transduced brain regions, and examples of a subset of these regions are depicted in Fig. 1. Throughout most cortical regions, we observed dense staining of large pyramidal neurons in deep cortical layers (5/6) and lighter staining in neurons in the more superficial layers (2/3). Furthermore, the morphology of the eGFP+ cells that we observed in cortical areas was consistent with neurons, but not other cortical cell types like astrocytes or microglia. In the frontal lobe, robust eGFP+ expression was seen in the dorsolateral prefrontal cortex (DPFC, Fig. 1d), orbitofrontal cortex (OFC, Fig. 1e), dorsal premotor cortex (DPMC, Fig. 1f), anterior cingulate cortex (ACC, Fig. 1g) and primary motor cortex (PMC, Fig. 1h). In the parietal and temporal lobes, we observed eGFP+ staining in the insular cortex (IC, Fig. 1i), the inferior and superior temporal cortices (ITC, Fig. 1j; STC, Fig. 1k), somatosensory cortex (SSC, Fig. 1l) and the rhinal cortex (RhC, Fig. 1m). Additionally, there was light eGFP staining in the parietal cortex (PPC, Fig. 1n) and in the parieto-occipital cortical area (PAR-OCC, Fig. 1o), but staining was largely absent in more posterior areas of the occipital cortex and in the cerebellum (not pictured).

In addition to transduction of AAV2.retro in several cortical areas with known striatal afferent projections, we also detected AAV2.retro transduction in many subcortical structures. eGFP+ staining was seen in the external and internal globi pallidi (GPe, Fig. 1p; GPi, Fig. 1q), the subthalamic nucleus (STN, Fig. 1r), the claustrum (CLS, Fig. 1s), the medial dorsal and lateral dorsal nuclei of the thalamus (THAL MD/LD, Fig. 1t), the reuniens nucleus of the thalamic midline group (THAL RE, Fig. 1u), the basolateral nucleus of the amygdala (AMY, Fig. 1v), and the substantia nigra pars compacta (SNpc, Fig. 1w). The morphology of eGFP+ cells throughout these structures suggested that neurons were exclusively transduced, except in the medial dorsal region of the GPe and the medial region of the CLS, where we also observed a low number of eGFP+ cells with glial morphology, suggesting a small amount of local medial and lateral diffusion from the putamen to sub-regions of these putamen-adjacent brain structures. Similarly, we postulate that the observed eGFP expression in the STN may have resulted from transport to this region resulting from primary transduction in the GPe.

Comparisons of AAV2.retro-GFP and AAV2-GFP reveal significant differences in patterns of cortical and subcortical transduction.
In order to further characterize and quantify the extent of retrograde transport by AAV2.retro, additional naïve adult rhesus macaques were injected with the parent serotype,

AAV2, expressing eGFP. AAV2-eGFP was delivered into the same coordinates of the caudate nucleus and the putamen and at the same volume and titer (Fig. 1a, Table 1). There were no adverse surgical events and all animals recovered fully post-infusion. Following a 4-week post-surgical interval, brains were collected and the biodistribution of the AAV2-eGFP virus was visualized via immunohistochemical staining for eGFP in coronal sections. Counts of eGFP+ cells were manually collected from the regions of the caudate and putamen directly adjacent to the injection sites, as well as in 4 cortical areas (DPFC, DPMC, ACC, SSC) and in 2 subcortical structures (AMY and THAL). These cortical and subcortical regions of interest (ROIs) were selected due to their known dense afferent connections with the striatum[43,44] and relevance for future disease modeling and therapeutic development in our laboratory. Figures 2a,b illustrate panels of eGFP immunohistochemical staining in these brain regions from representative surgical cases and highlight a clear lack of AAV2 retrograde transport to these extra-striatal regions (bottom row) compared to AAV2.retro (top row). A 2-way ANOVA was used to compare cell counts between serotypes (AAV2.retro, AAV2) and ROIs (Cd, Put, AMY, THAL, DPFC, DPMC, ACC, SSC). These analyses revealed significant main effects of serotype, $F(1,18) = 21.847$ $p < 0.0001$, and of ROI, $F(8,18) = 94.238$ $p < 0.0001$, but no interaction, $F(8,18) = 1.500$ $p = 0.225$. To further investigate these significant effects, we first conducted planned comparisons between serotypes for each ROI. Figure 2c illustrates these cell count comparisons separately for each ROI and serotype. Serotypes were compared for each ROI using one-tailed, independent-Samples t-tests. The results indicated that AAV2.retro-eGFP transduced significantly more cells than AAV2-eGFP in all of the extra-striatal ROIs: AMY ($t(2) = 82.98$, $p < 0.0001$), THAL ($t(2) = 3.656$, $p = 0.0337$), DPFC ($t(2) = 79.66$, $p < 0.0001$), DPMC ($t(2) = 118.4$, $p < 0.0001$), ACC ($t(2) = 9.007$, $p = 0.0061$), SSC ($t(2) = 3.942$, $p = 0.0294$). On average, AAV2.retro-eGFP resulted in 7-fold higher levels of transduction in the putamen, and 3.5-fold higher transduction in the caudate, compared to extra-striatal ROIs.

Next, we compared cell counts between ROIs for each serotype separately by one-way ANOVA with planned comparisons using one-tailed independent sample t-tests. The results indicated that the number of eGFP+ cells differed significantly depending on brain region for both AAV2.retro ($F(8,9) = 73.936$, $p < 0.0001$) and AAV2 ($F(8,9) = 38.639$, $p < 0.0001$). Post-hoc comparisons revealed significantly higher cell counts in the putamen than in the caudate for both AAV2.retro ($p = 0.0003$) and AAV2 ($p = 0.0018$), and significantly higher cell counts in both of the injected regions than any of the other regions for AAV2 and AAV2.retro (all p-values < 0.05). The higher cell count in the putamen versus the caudate is intuitive given the substantially larger volume of vector injected into the putamen (150 μl) compared to the caudate (80 μl) for both serotypes. There were no significant differences in cell counts between any of the other regions for both serotypes (all p-values n.s.). The results of these comparisons are reported in detail in Supplemental Table S1.

Additionally, there were no significant differences in cell counts between AAV2 and AAV2.retro in the caudate ($t(2) = 0.497$, $p = 0.334$) or putamen ($t(2) = -0.680$, $p = 0.283$), suggesting similar levels of transduction between serotypes in the regions directly adjacent to the injection sites. Interestingly, even though the cell counts were similar directly adjacent to the injection sites, we observed robust differences between AAV2 and AAV2.retro in the amount of spread within the putamen from the site of injection. In particular, AAV2 spread throughout the putamen to a far greater extent than AAV2.retro, resulting in much larger regions of transduction clearly visible in multiple coronal sections, Fig. 2a, bottom row. To assess these serotype-based differences, we quantified the spread of each vector in the injected regions of the caudate and putamen using the Area Fraction Fractionator tool (MBF Bioscience), calculating the area of eGFP+ cells per area of each structure. Figure 2d illustrates these measurements, which were compared using a 2-way ANOVA (Serotype x ROI). The results revealed a significant Serotype*ROI interaction, $F(1,4) = 19.57$, $p = 0.012$, as well as significant main effects of Serotype ($F(1,4) = 22.85$, $p = 0.009$), and ROI ($F(1,4) = 13.30$, $p = 0.022$). Planned comparisons using one-tailed t-tests indicated that the area of transduction was significantly larger in the AAV2-injected putamen than the AAV2.retro-injected putamen, $t(2) = 75.37$, $p < 0.0001$, whereas the area of transduction did not significantly differ between AAV2-injected caudate and AAV2.retro-injected caudate, $t(2) = 0.18$, $p = 0.437$. There were additional differences such that AAV2 spread over a larger area of the putamen than the caudate, $t(2) = 5.492$, $p = 0.016$, whereas AAV2.retro had similar spread in both of the injected regions $t(2) = 0.5726$, $p = 0.312$.

While the parent serotype, AAV2, does not exhibit significant retrograde transport, as evidenced here, we did note some minimal eGFP transduction in AAV2-eGFP injected animals in regions that receive projections from the caudate and putamen, including the substantia nigra, pars reticulata and both segments of the globus pallidus (both fibers and cell bodies), indicating anterograde transport. In comparison, while we noted cells in the globi pallidi in AAV2.retro injected macaques, we did not find evidence of transduction of the substantia nigra, pars reticulata.

As described above, AAV2.retro-eGFP injections resulted in eGFP+ staining in many cortical and subcortical structures in addition to the eight regions used for the cell counting analysis. Since brain-wide manual cell counting is beyond the scope of this study, we performed a qualitative ranking to assess eGFP staining density in each of the extra-striatal brain regions where staining was found, relative to one another. Regions were rated as having either high, mid or low-level staining density (or no staining) and ratings are reported in Table 2. To depict brain-wide differences between the two serotypes, and to highlight the pattern of AAV2.retro biodistribution in the rhesus macaque brain following intra-striatal injection, the ranked transduction patterns for each serotype are illustrated in a cartoon brain graphic generated using an in-house rhesus macaque T2-weighted MRI template/atlas to define each transduced region and then visualized graphically using paraView 5.7.0 software (Fig. 3)[45]. High-level transduced brain regions are depicted in dark blue, mid-level regions are depicted in royal blue, lower-level regions are depicted in turquoise, and regions with minimal to no staining are shown in gray. Injected ROIs are depicted in yellow for reference. AAV2.retro transduction largely followed an anterior to posterior gradient, with the highest levels of eGFP expression in the frontal lobe (pre-frontal and motor areas) and mid to low level staining in the temporal and parietal lobes, respectively. No discernable eGFP staining was detected in the occipital lobe nor the cerebellum.
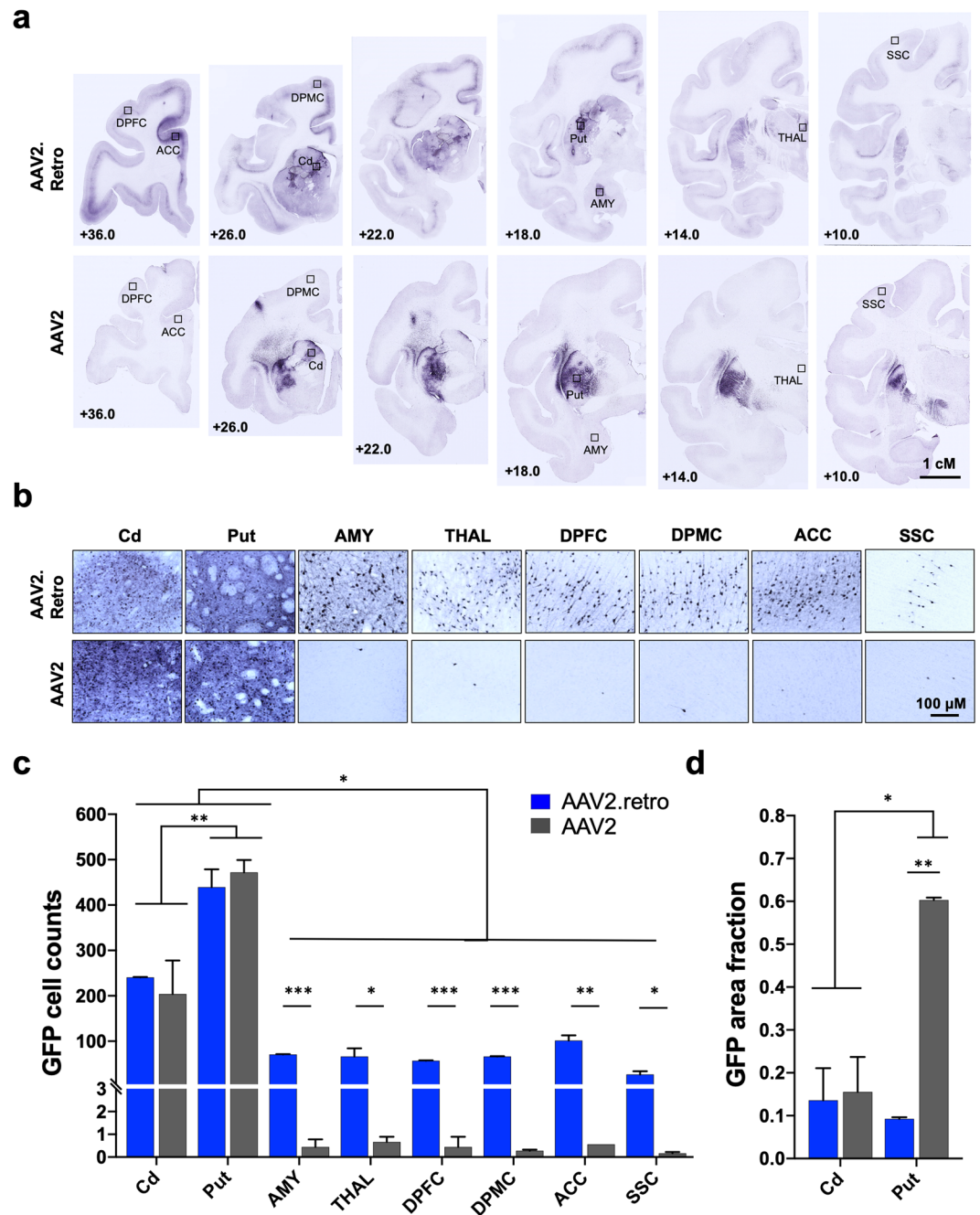
Figure 2. AAV2.retro-mediated retrograde transport is significantly higher compared to the parent serotype, AAV2. (**a**) Low and (**b**) high power photomicrographs of eGFP-stained, rhesus macaque coronal brain sections following injection of AAV2.retro-eGFP (top panel) or AAV2-eGFP (bottom panel) into the caudate and putamen. Rectangles in (**a**) illustrate the brain regions selected for high power photomicrographs displayed in (**b**). (**c**) Cell count analysis demonstrating significantly more GFP+ cells in the putamen compared to the caudate, irrespective of serotype, as well as significantly more GFP+ cells detected in extra-striatal regions in animals injected with AAV2.retro-eGFP compared to AAV2-eGFP. (**d**) Area fraction fractionator analysis showing a significantly higher area fraction of GFP positivity in the putamen in animals injected with AAV2-eGFP compared to AAV2.retro-eGFP. Error bars in both graphs represent standard error of the mean (SEM). Abbreviations: ACC (anterior cingulate cortex), AMY (amygdala), Cd (caudate), DPFC (dorsal prefrontal cortex), DPMC (dorsal premotor cortex), Put (putamen), SSC (somatosensory cortex), THAL (thalamus). *$p < 0.05$, **$p < 0.01$, ***$p < 0.001$. Scale bar 2a = 1 centimeter, Scale bar 2b = 100 microns. Graphs were made in GraphPad Prism for Mac, Version 8.

Intra-striatal injection of AAV2.retro -mHTT leads to mHTT expression and related pathology throughout multiple functional circuits in the cortico-basal ganglia network. To evaluate the capability of AAV2.retro to deliver disease-associated cargo to biologically relevant circuits in the NHP brain,
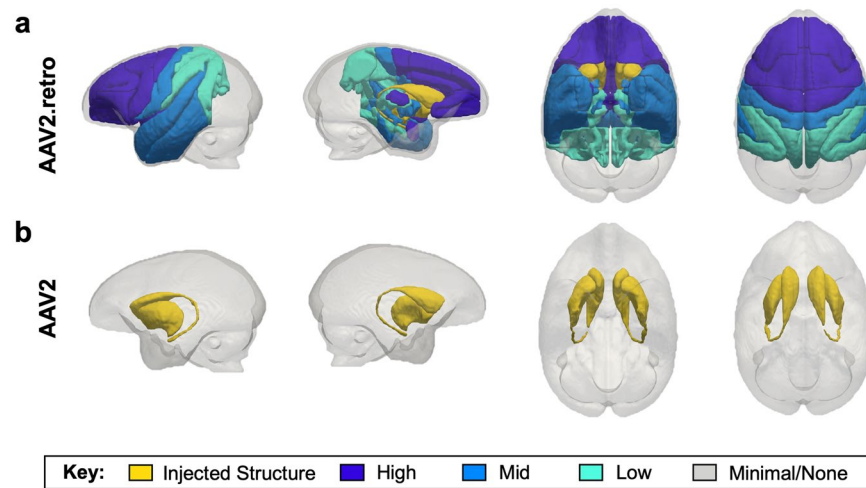
Figure 3. Cartoon graphic illustrating the brain-wide transduction patterns for AAV2.retro and AAV2. The 'glass brain' graphic was generated from an in-house rhesus macaque T2-weighted MRI template and visualized using paraView software[45]. Levels of transduction were ranked based on eGFP expression in each brain region, relative to one another. High-level transduced brain regions are depicted in dark blue, mid-level regions are depicted in royal blue, lower-level regions are depicted in turquoise, and regions with minimal to no staining are shown in gray. Injected ROIs are depicted in yellow for reference. (**a**) The density of AAV2.retro transduction largely followed an anterior to posterior gradient, with the highest levels of staining in the frontal lobe (pre-frontal and motor areas) and mid to low level staining in the temporal and parietal lobes, respectively. Minimal to no staining was detected in the occipital lobe nor the cerebellum. (**b**) AAV2 transduction was primarily restricted to the injected regions. 3-dimensional brain regional surface meshes were generated using ITK-SNAP software, version 3.8.0 and subsequently visualized with paraView software, version 5.7.0.

naïve adult rhesus macaques were injected with AAV2.retro expressing a pathogenic fragment of human mutant huntingtin protein (mHTT) bearing 85 CAG repeats (AAV2.retro-HTT85Q) into the head of the caudate and the putamen. mHTT85Q expression was driven from a chicken beta-actin promoter with a CMV early enhancer element (CAG promoter). See Fig. 4a for a vector diagram and Fig. 4b for a cartoon of the unilateral surgical injection sites. To improve localized spread within the injected regions, we increased the number of injection sites in the caudate to 2 (one pre-commissural; one post-commissural) and increased the volume of injection for each structure (see Table 1 for summary of surgical parameters). Additionally, we increased the post-surgical interval from 4- to 10-weeks post-surgery to allow enough time for the formation of pathological mHTT protein aggregates. There were no adverse surgical events and all animals recovered fully post-infusion. At 10-weeks post-surgery, brains were collected and the biodistribution of intracellular mHTT was visualized in coronal sections via immunohistochemical staining using the anti-mHTT 1-82aa antibody (1-82aa). We observed 1-82aa+staining in the head of the caudate (Fig. 4c) and putamen (Fig. 4d), confirming the formation of aggregated intracellular mHTT aggregates in these structures. We also observed 1-82aa+ staining in dozens of cortical regions and subcortical structures, with examples shown here including the AMY (Fig. 4e), THAL (Fig. 4f), DPFC (Fig. 4g), DPMC (Fig. 4h), ACC (Fig. 4i), and the SSC (Fig. 4j). See Supplemental Table S2 for summary of all regions in which we detected the formation of mHTT 1-82aa+ aggregates. In general, the brain-wide distribution of intracellular aggregates largely mirrored that of the eGFP+ staining that we described in the earlier cases reported here, with a few limited exceptions. Notably, we observed dense mHTT aggregates in the STN and claustrum, regions in which we observed somewhat lower relative levels of eGFP transduction. These variations could be due to differences in the volumes and locations of the AAV2.retro-eGFP and AAV2.retro-HTT85Q injections, and/or the result of retrograde transport from regions outside of the striatum that were reached by diffusion from the injection sites, such as the GPe. We stained coronal brain sections using the anti-microglial antibody ionized calcium-binding adapter molecule 1 (Iba1) to investigate a potential immune response to the AAV2.retro vector or to the mHTT transgene expression. We found activated Iba1+ microglia in the needle tracts of the caudate and putamen; however, no diffuse microgliosis was seen throughout the injected brain regions nor in any of the striatal afferent brain regions expressing mHTT at 10-weeks post injection. Similarly, inspection of anti-neuronal nuclei (NeuN)-stained tissue showed no qualitative loss of neurons in any brain regions.

To investigate the cell-type specificity of mHTT expression, we next compared the injected regions of the caudate and putamen versus transduced striatal afferents using double-label immunofluorescence. The examples shown in Fig. 4k-v are from the putamen (left panel) and the DPMC (right panel), but are representative of the other injected region as well as the other striatal afferents that also exhibited mHTT expression. Co-localization of mHTT 1-82aa+/NeuN+ staining was used to identify transduced neurons, and mHTT 1-82aa+/GFAP+ staining was used to identify transduced astrocytes. In the putamen, we detected co-localization of mHTT with both neurons (Fig. 4k–m) as well as astrocytes (Fig. 4q–s), although astrocyte transduction was far less prevalent. In contrast, we only detected transduced neurons in cortical striatal afferents including the DPMC (Fig. 4n–p) but did not detect examples of transduced astrocytes (Fig. 4t–v). These data suggest that AAV2.retro was transported
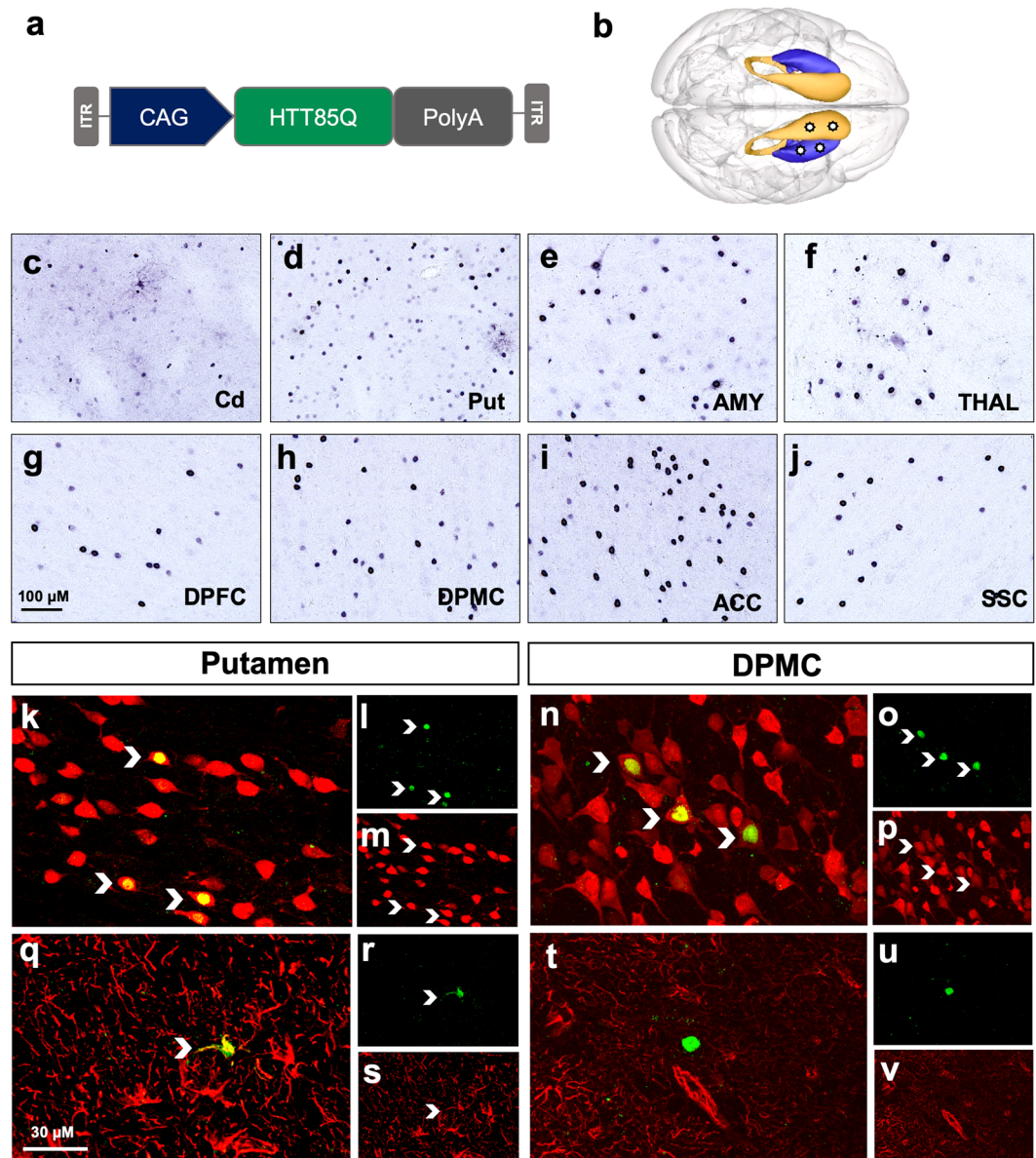
Figure 4. AAV2.retro-mediated delivery of mHTT into the rhesus macaque striatum leads to aggregate formation in many disease-relevant brain regions. (**a**) AAV2.retro vector cartoon and (**b**) surgical injection graphic depicting unilateral injection sites of AAV2.retro-HTT85Q into the caudate and putamen. 1-82aa staining of mHTT protein showing mHTT$^+$ aggregates in the caudate (**c**), putamen (**d**) and several cortical and subcortical brain regions. Examples shown here include the AMY (**e**), THAL (**f**), DPFC (**g**), DPMC (**h**), ACC (**i**) and SSC (**j**). Double label immunofluorescence of HTT 1-82aa/NeuN (**k–p**) and HTT 1-82aa/GFAP (**q–v**) in the injection site (putamen, left panel) and a distal brain region (DMPC, right panel). Transduced neurons and astrocytes are indicated with chevrons. Abbreviations: ACC (anterior cingulate cortex), AMY (amygdala), Cd (caudate), DPFC (dorsal prefrontal cortex), DPMC (dorsal premotor cortex), Put (putamen), SSC (somatosensory cortex), THAL (thalamus). Scale bar in g = 100 microns, scale bar in q = 30 microns. Brain graphic in 4b was made using the 3d Brain Composer feature on the Scalable Brain Atlas website (https://scalablebrainatlas.incf.org/composer/?template=CBCetal15).

to these distal regions through uptake at the nerve terminal in the striatum and transported back to the cell body, rather than via long-range diffusion from the injection sites.

Broadly, the observed pattern of AAV2.retro-HTT85Q biodistribution resulted in HD-pathology throughout the same circuits of the cortico-basal ganglia network that were targeted via AAV2.retro-eGFP delivery into the caudate and putamen. Moreover, the pattern of transgene expression shown here models the distribution of mHTT protein and aggregate formation seen in patients with HD, where cognitive, sensorimotor and limbic cortico-basal ganglia circuits are each affected, leading to the wide array of complex symptoms. A schematic summarizing each brain region that was transduced by AAV2.retro following intra-striatal delivery, and then placed into the framework of functional cortico-basal ganglia circuits, is shown in Fig. 5. In brief, we observed
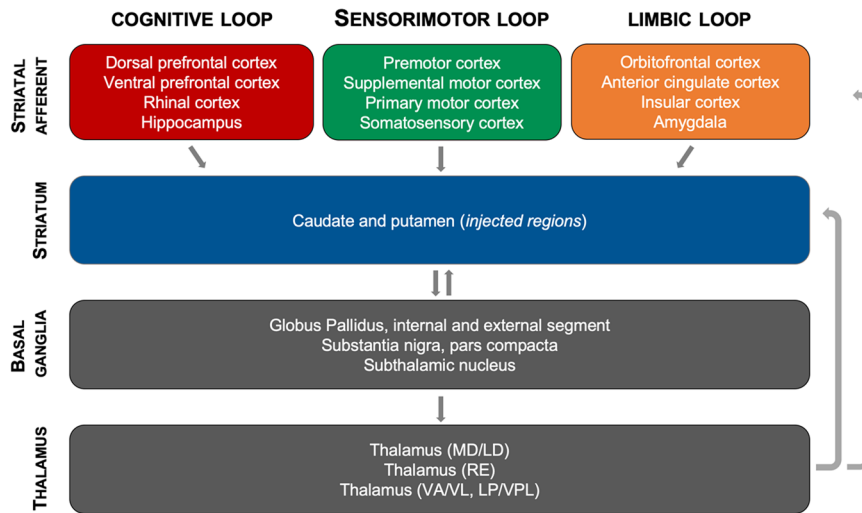
Figure 5. Schematic of the functional cortico-basal ganglia circuits targeted via intra-striatal delivery of AAV2. retro. Delivery of AAV2.retro into the caudate and putamen leads to transgene expression (both eGFP and mHTT85Q) in dozens of highly interconnected brain regions comprising cognitive, sensorimotor and limbic cortico basal ganglia functional neural networks. Schematic was created using Microsoft Powerpoint for Mac, version 16.35.

transduction in cognitive circuits that include the dorsal and ventral prefrontal cortices, rhinal cortex and the hippocampus; in sensorimotor circuits that include premotor, supplemental motor, primary motor and soma-tosensory cortices, and in limbic circuits that include the temporal, cingulate, and orbitofrontal cortices and the amygdala. In addition, we observed AAV2.retro transduction in regions of the basal ganglia and thalamus that were presumably reached by our vector via their afferent projections to the striatum (SNpc, THAL) and/or by diffusion/transport from the nearby injection sites (GPe, STN). Taken together, these results highlight that the retrograde capabilities of AA2.retro enable the delivery of viral constructs simultaneously to dozens of brain regions comprising multiple functional brain circuits from injections into two focal brain regions.

Discussion

The results reported here provide clear evidence of extensive retrograde transport in the rhesus macaque brain by a newly derived AAV2 capsid variant, AAV2.retro[32]. The brain-wide biodistribution pattern of AAV2.retro following intrastriatal injection was significantly more widespread than that of its parent serotype, AAV2, with AAV2.retro transducing cells throughout the cortico-basal ganglia network and AAV2 transducing cells pri-marily limited to the targeted regions of the caudate and putamen, with some evidence of minimal anterograde transport to the globus pallidus and substantia nigra, pars reticulata. The findings here in adult rhesus macaques closely recapitulate those previously reported in adult mice following intra-striatal delivery of similar AAV2.retro constructs[32], and indicate that the mechanism of retrograde transport used by AAV2.retro is conserved across species.

We observed clear serotype differences of vector spread in the region of injection, with AAV2 transducing a significantly larger area of the putamen compared to AAV2.retro. A likely interpretation for this finding is that, because such a large proportion of the infused AAV2.retro viral particles were taken up at the injection sites by nerve terminals and transported to distal brain regions, fewer AAV2.retro viral particles were available to dif-fuse into the surrounding regions of the caudate and putamen. Future studies employing these vectors to target multiple brain structures or circuits might be able to take advantage of each of these features by combining both serotypes into a single bolus infusion in order to maximally transduce the area of injection with AAV2, yet also benefit from the enhanced retrograde functionality of AAV2.retro.

It is noteworthy that other AAV serotypes exhibit low to moderate levels of retrograde transport, such as AAV1[46,47] and AAV6[48], but by comparison the degree of retrograde transport is greatly enhanced in AAV2. retro[32]. There are, however, other AAV capsid variants that have been recently reported to also transport robustly in the NHP brain, such as AAV-HBKO[49]. Naidoo and colleagues demonstrated that intra-thalamic delivery of AAV-HBKO expressing eGFP resulted in robust anterograde transport to deep layers of many cortical regions with thalamic efferents including the ACC, DPFC, VPFC, DPMC, VPMC, PMC, SSC, and ITC. The authors also report evidence of moderate retrograde transport to some subcortical structures and to regions of the brain stem and spinal cord[49]. This contrasts with the pattern of nearly exclusive retrograde transport seen here with AAV2. retro, as well as transduction of both deep and superficial layers of cortex. Our findings reflect the known cortical afferent inputs into the caudate and putamen which have been previously characterized in tracer studies showing innervation from both deep and superficial layers. Together, these two studies illustrate the feasibility of using novel, designer AAV serotypes with a high propensity for axonal transport to distribute genetic cargo throughout brain circuits by targeting specific structures with a high degree of connectivity in the CNS, such as the thala-mus and the striatum. For example, in the current study we demonstrated that AAV2.retro efficiently transduces

cognitive, sensorimotor, and limbic cortico-basal ganglia circuitry via intra-striatal delivery, and the work by Naidoo and colleagues with AAV-HBKO demonstrated biodistribution throughout a different network of pre-frontal, motor, temporal, and subcortical regions following thalamic infusion[49,50]. Taken together, these studies illustrate how widespread transduction patterns can be achieved even in the large NHP brain by selecting a serotype with high propensity for transport and by selectively choosing the site of injection to target specific populations of neuronal afferents/efferents depending on the network of interest or specific disease being targeted.

Additional work has explored the merits of more systemic administration routes with the potential to increase brain-wide AAV biodistribution. One approach has been to employ capsids capable of crossing the blood brain barrier (BBB), such as AAV9[51] and AAV.PHPb[52]. Work with these capsids indicates that they transduce broad regions of the CNS when administered intravenously (IV), but with relatively low efficiency compared to intra-parenchymal delivery[51–53]. Recent work from our group shows that intra-CSF administration of AAV-PHP.b in NHPs leads to greater neuronal and astrocytic transduction compared to intravascular infusion. However, transduction was still significantly greater in cortical areas compared to subcortical brain regions[53]. In contrast, intraparenchymal delivery of vectors like AAV2.retro and AAV-HBKO can target widespread brain regions that encompass both cortical and subcortical structures. Hence, these and other new capsid variants capable of enhanced axonal transport may offer a method to target widespread neuronal circuits, with both greater efficiency and selectivity. The downside to this strategy compared to intra-IV and intra-CSF delivery techniques, however, is a more complex and invasive surgery.

With the advancement of neuroimaging techniques, it has become apparent that many neurological diseases are characterized by dysfunction on the level of brain networks, rather than individual structures. For example, while in HD the caudate and putamen are profoundly affected, severe dysfunction is also apparent in other basal ganglia structures and in several motor, cognitive, and limbic cortical areas as well[39–41,54]. Likewise, the hippocampus is known to be particularly vulnerable in Alzheimer's Disease, but atrophy also occurs in brain regions throughout the temporal, prefrontal, and parietal cortices, as well as the thalamus[55,56]. Therefore, an important limitation to current gene-therapy approaches for these disorders are that they do not target the entire dysfunctional network. Although the approaches targeting single brain regions are predicted to offer some therapeutic benefit to patients based on pre-clinical animal research, it is logical to postulate that treating the entire dysfunctional network, rather than just one structure, could result in greater therapeutic benefit.

In summary, the studies reported here show that AAV2.retro exhibits robust retrograde transport when injected into the NHP striatum, a phenomenon that was first demonstrated using a control eGFP transgene and then verified by expressing a disease-causing gene, mHTT, as a proof of concept. The transport and widespread gene delivery were well-tolerated and did not lead to adverse pathological events nor neurological symptoms in any animals, at least out to the four- and ten- week study timelines conducted here. Efforts to characterize the structural and functional consequences of AAV2.retro-mediated delivery of mHTT to these cortico-basal ganglia circuits in a larger cohort of rhesus macaques over a longer timeframe are ongoing. The dearth of genetically and biologically relevant large animal models of disease has been identified as a significant limitation hampering the translation of new scientific discoveries to the clinic. There is an immense cost and effort required to generate and maintain lines of transgenic NHPs and the work presented here represents some of the first to test the potential for this new AAV serotype to become a tool for the rapid generation of novel NHP models of neurodegenerative disease, something for which there is great interest in the biomedical research community. Additionally, our findings offer a solid framework for future studies in large animal models and human patients using AAV2.retro as a gene therapy tool to deliver therapeutics for myriad brain disorders, particularly those where targeting multiple brain regions and/or circuits would result in a better clinical outcome for the patient including HD, PD, AD, amyotrophic lateral sclerosis, lysosomal storage diseases, among others.

Materials and Methods

Subjects. Six adult female rhesus macaques were involved in this study (age 7–16). Animals were selected based upon their negative neutralizing antibody status for AAV2. Monkeys were pair -housed on a 12-hour light/dark cycle lighting schedule, provided with monkey chow rations twice daily, and given ad libitum access to water. Animals were also provided with fruit and vegetable enrichment daily. Macaques were observed daily by trained veterinary technicians, and all experimental procedures were approved by the Institutional Animal Care and Use Committee and the Institutional Biosafety Committee at the Oregon National Primate Research Center and Oregon Health and Science University. All guidelines specified in the National Institutes of Health Guide for the Care and Use of Laboratory Animals were strictly followed.

Vector preparations. Recombinant AAV vectors were generated by a scalable co-transfection procedure in the OHSU/ONPRC Molecular Virology Support Core. pAAV2.retro capsid plasmids were kindly provided by the Karpova lab at the Howard Hughes Medical Institute (HHMI), Janelia Research Campus via a Material Transfer Agreement with OHSU. Plasmids containing the N171 N-terminal fragment sequence of human HTT bearing 85 CAG repeats were manufactured at Genscript and subsequently cloned into a transgene cassette flanked by viral ITRs. pAAV2 capsid plasmids were supplied by the OHSU/ONPRC Molecular Virology Support Core. Viral vector preparations were prepared as described previously[53]. Briefly, mammalian HEK293 producer cells were transfected with plasmids carrying the transgene cassette flanked by viral ITRs (sspAAV-CMV-eGFP, sspAAV-CAG-HTT85Q), a rep-cap expression construct encoding the sequence for the AAV2.retro or AAV2 serotype capsid, and a helper plasmid expressing adenoviral E2a, VA, and E4-orf6. Viral lysates were treated with Benzonase to remove residual plasmid, and virus was purified over an Iodixanol step gradient. Gradient fractions containing intact virus and excluding empty particles were harvested, and the final virus preparation was buffer-exchanged into DPBS + 5% glycerol+35 mM NaCl. Quality control was performed to ensure purity by viral capsid protein evaluation with silver staining on SDS-PAGE. Viral titers for AAV2.

retro-HTT85Q were determined by quantitative PCR of purified vector particles using a CAG primer/probe set: Forward: 5′-CCATCGCTGCACAAAATAATTAAAA-3′, Reverse: 5′-CCACGTTCTGCTTCACTCTC-3′, Probe: 5′-CCCCTCCCCACCCCCAATTTT-3′. Viral titers for AAV2-eGFP were determined by quantitative PCR of purified vector particles using a viral ITR primer/probe set: Forward: 5′-GGAACCCCTAGTGATGGAGTT-3′, Reverse: 5′-CGGCCTCAGTGAGCGA-3′, Probe: 5′- CACTCCCTCTCTGCGCGCTCG-3′.

Neutralizing antibody assay. Whole blood was obtained in Vacutainer Serum Collection Tubes (Becton Dickinson) and serum was collected following centrifugation at 1500 rcf/g for 10 min and stored at −80C until analysis. Neutralizing antibody screening assays were carried out as previously described[53]. Briefly, assays were performed in 96 well format with 5×10^4 CHO-Lec2 cells per well. Serial dilutions of study participant serum were pre-incubated with 1×10^9 genome copies of AAV2 reporter virus for 1 hour at 37 °C and then added to cells that were infected with Adeno Helper virus. After 48 hours, Promega Bright-Glo substrate was added to the cells and luciferase expression was quantified using the Biotek Synergy Mx luminometer. Both positive and negative monkey sera controls were included with each assay. All animals selected for the study had less than 50% inhibition of transduction when serum was diluted to 1:20.

Neuroimaging. On the day of surgery, all monkeys received MRI scans to determine coordinates for the AAV injections. Anesthesia was first induced with Ketamine HCl (10 mg/kg IM), followed by maintenance anesthesia with isoflurane gas vaporized in 100% oxygen. Animals were placed in a MRI-compatible, NHP-specific stereotaxic frame (Crist) in which they remained for the duration of the scan and subsequent surgery. A twelve-minute, T1-weighted scan was collected on a Siemens Prisma scanner using a surface coil. Brain images were subsequently examined using Osirix software and the injection coordinates were selected and transferred from MRI-space to stereotaxic surgical space. Monkeys were taken directly from the MRI to the operating room following their scan.

Stereotaxic surgery. Pre-operative care consisted of overnight food restriction for 12 hours and general examination to ensure that patient health was adequate to withstand the procedure. Local anesthetic was injected subcutaneously along the incision site and the skull was prepared for incision. Four small craniotomies (roughly 0.5 cm in diameter each) were made using an air drill to expose the dura, and a 100 µl Hamilton syringe fitted with a 25 gauge needle was mounted on the micromanipulator of the stereotaxic instrument. A suspension of AAV (1×10^{12} vg/ml) that encodes eGFP or a fragment of mHTT was injected through the 100 µl Hamilton syringe connected to a Quintessential Stereotaxic Injector pump. The infusion rate began at 0.5 µl/min then increased by 0.5 µl every 5 minutes. This progressive increase in infusion rate is known as convection enhanced delivery, and it improves the spread of infusate compared to conventional infusion methods[29,30]. The needle was left in place for an additional 5 min to allow the injectate to diffuse from the needle tip before removing. For the eGFP studies, monkeys received a total of 3 microinjections per hemisphere: one into the anterior head of the caudate nucleus (80 µl), one into the anterior putamen (80 µl) and a third in the post-commissural putamen (70 µl). A total of 2.3×10^{11} vector genomes were injected per hemisphere (see Table 1 for summary of each surgical case). For the mHTT studies, we increased the number of injection sites in the caudate to improve spread within the structure such that these monkeys received 4 microinjections per hemisphere (anterior head of caudate, 80 µl; posterior head of caudate, 40 µl; anterior putamen, 95 µl; post-commissural putamen, 85 µl). A total of 3×10^{11} vector genomes were injected per hemisphere. After microinjections were completed, the skull opening was filled with gelfoam, the incision closed, and the animal monitored closely during recovery. Post-operatively, animals were monitored for 5–7 days by veterinary staff and received Cefazolin, Hydromorphone, and Buprenorphine (antibiotic and pain management).

Necropsy/tissue collection. Necropsies and tissue collection were performed as previously described[53]. Briefly, animals were sedated with Ketamine and then deeply anesthetized with sodium pentobarbital followed by exsanguination. Brain and spinal cord were perfused with 2 L of cold, sterile 0.9% saline. Brain was removed from the skull, placed into an ice-cold, steel rhesus macaque brain matrix and blocked into 4-mm-thick slabs in the coronal plane. Brain slabs were subsequently post fixed in 4% paraformaldehyde for 48 hours then cryoprotected in 30% sucrose for subsequent histological analyses.

Tissue processing/staining. Cryoprotected tissue was sectioned at 40 microns in the coronal plane on a freezing microtome. For immunohistochemical staining, sections were incubated with antibodies against eGFP (Invitrogen, A6455, 1:1000) or mHTT protein (1-82aa, Millipore, MAB5492, 1:500), and the appropriate biotinylated goat anti rabbit or goat anti mouse secondary antibody (Vector Laboratories, BA-1000, BA-9200, 1:500). The signal was developed using a standard Vectastain ABC kit (Vector Laboratories, PK6100) with subsequent incubation in 3,3′-Diaminobenzidine (DAB) (Sigma, 112080050) and Nickel (II) Sulfate Hexahydrate (Sigma, N4882) for signal intensification. For double labelling, sections were incubated overnight at room temperature with an antibody against mHTT protein (1-82 aa, Millipore, MAB5492 1:500), and either NeuN (Millipore, ABN78, 1:500) or GFAP (DAKO, 20334, 1:1000). The sections were then incubated for one hour with a goat anti mouse AlexaFluor 488 conjugated secondary antibody (Invitrogen, A11029, 1:500), and a goat anti rabbit AlexaFluor 546 conjugated secondary antibody (Invitrogen, A11035, 1:500) as previously described[57].

Microscopy. 20X Images for Fig. 1, Fig. 2b, and Fig. 4c-j were taken on an Olympus BX51 microscope with an Olympus DP72 camera controlled by the CellSens program. Brightfield Images for Fig. 2a were acquired on an Olympus VS120 Slide scanner utilizing an Olympus BX61VS microscope. An Allied Vision VC50 camera captured single Z-plane images through a 10x objective. For double label fluorescence in Fig. 4k-v, a Leica SP5

confocal microscope with a 63x oil immersion objective was used along with the corresponding LAS AF program. The gain and exposure parameters were optimized for each confocal image.

Measures of viral transport/expression. *Cell counts.* To characterize the biodistribution of AAV2 or AAV2.retro following injections into the striatum, we first identified regions of interest (ROIs) in the right hemisphere of the caudate (Cd), putamen (Put), amygdala (AMY), thalamus (THAL), dorsal prefrontal cortex (DPFC), dorsal premotor cortex (DPMC), anterior cingulate cortex (ACC), and somatosensory cortex (SSC). The contralateral hemisphere was used for molecular studies not described in the current manuscript. For each monkey, we collected three 10x IHC images stained for eGFP from 3 consecutive coronal sections from each of these ROIs (for a total of 9 images per region, per animal). 10X images of caudate and putamen were obtained adjacent to the sites of injection. The number of eGFP$^+$ cells in each image was manually counted using ImageJ and averaged across the 9 images for each structure.

Ratings of relative staining density. We observed eGFP$^+$ staining in many additional brain areas beyond the 8 ROIs in which cells were counted. We ranked the relative levels of transduction between brain areas to more fully characterize the biodistribution of AAV2.retro-eGFP. Brain regions, defined using the anatomical boundaries of Saleem & Logothetis[42], were assigned the rank of high, mid, or low, depending on the relative level of transport based on the density of GFP$^+$ cells in each ROI. The same ranking scheme was applied to coronal sections from animals injected with the AAV2.retro-HTT85Q construct and stained with 1-82aa.

Area fraction fractionator. The Area Fraction Fractionator (MBF Bioscience) was used to quantify the area fraction of eGFP$^+$ cells in the putamen and caudate. Three 40-Micron thick coronal sections were chosen for each brain region to capture an anterior to posterior representation of the transduced regions. Coordinates of sections according to the atlas by Saleem and Logothetis were A-P: +28.0, +24.0, +21.0, and +17.0. Images captured at 10x on a VS120 slide scanner were uploaded to the Stereo Investigator program and the region of interest was outlined manually. One marker was used to select points that fell within the region of interest, and a second marker was used to select points containing eGFP-positive cells. The counting frame area was 1200 × 1200 μm, XY placement was 2000 × 2000 μm, and grid spacing was 50 μm. The area fraction estimation of eGFP$^+$ cells in the caudate and putamen was determined by dividing the area of eGFP$^+$ cells by the total area analyzed for each brain region.

Statistical analysis. All statistical analyses and graph preparation were completed using GraphPad Prism software version 8. To assess group differences in vector biodistribution, we first compared the numbers of GFP$^+$ cells, or the area fraction of GFP$^+$ cells, in each brain ROI using 2-way ANOVAs (Serotype x ROI). Subsequently, we ran planned comparisons between brain regions and serotypes using one-tailed, independent-sample t-tests for each comparison.

3D brain visualization graphics. The graphics in Figs. 1 and 4 depicting surgical injection sites were created by the authors using the Scalable Brain Atlas Website at scalablebrainatlas.incf.org/macaque/CBCetal15. We viewed and rendered the Calabrese *et al.* (2015) rhesus macaque brain atlas in 3D using the "3d brain composer" function. We then selected contrasting colors for the caudate and putamen specifically. Surgical target sites were added using Microsoft Powerpoint for Mac, Version 16.35. As part of ongoing studies in the lab, we created an MRI template from T2w SPACE scans collected from 18 healthy adult male and female rhesus macaques. Cortical and subcortical ROIs were manually defined on the template using ITK-SNAP[58] according to the anatomical boundaries described by Saleem & Logothetis[42]. Next, ITK-SNAP was used to generate a 3-dimensional surface mesh for each ROI. For Fig. 3, the surface meshes were subsequently visualized with paraView 5.7.0 software[45] and shaded according to the qualitative ranking of staining density: high-level transduced brain regions were shaded dark blue, mid-level regions were shaded royal blue, lower-level regions were shaded turquoise, regions with minimal to no staining were shaded gray, and injected ROIs (caudate and putamen) were shaded yellow. The graphic in Fig. 5 was created using Microsoft Powerpoint for Mac, version 16.35.

Data availability
The authors will make all materials, data and associated protocols generated as part of this publication available to readers upon request.

References

1. Samulski, R. J. & Muzyczka, N. AAV-Mediated Gene Therapy for Research and Therapeutic Purposes. *Annu. Rev. Virol.* **1**, 427–451 (2014).
2. Aschauer, D. F., Kreuz, S. & Rumpel, S. Analysis of transduction efficiency, tropism and axonal transport of AAV serotypes 1, 2, 5, 6, 8 and 9 in the mouse brain. *PLoS One* **8**, e76310 (2013).
3. Atchison, R. W., Casto, B. C. & Hammon, W. M. Adenovirus-Associated Defective Virus Particles. *Science* **149**, 754–756 (1965).
4. Wu, Z., Asokan, A. & Samulski, R. J. Adeno-associated virus serotypes: vector toolkit for human gene therapy. *Mol. Ther.* **14**, 316–327 (2006).
5. Lisowski, L., Tay, S. S. & Alexander, I. E. Adeno-associated virus serotypes for gene therapeutics. *Curr. Opin. Pharmacol.* **24**, 59–67 (2015).
6. Srivastava, A. *In vivo* tissue-tropism of adeno-associated viral vectors. *Curr. Opin. Virol.* **21**, 75–80 (2016).
7. Gao, G. *et al.* Clades of Adeno-associated viruses are widely disseminated in human tissues. *J. Virol.* **78**, 6381–6388 (2004).
8. Gao, G. P. *et al.* Novel adeno-associated viruses from rhesus monkeys as vectors for human gene therapy. *Proc. Natl Acad. Sci. U S Am.* **99**, 11854–11859 (2002).

9. Grimm, D. *et al*. Preclinical *in vivo* evaluation of pseudotyped adeno-associated virus vectors for liver gene therapy. *Blood* **102**, 2412–2419 (2003).

10. Hocquemiller, M., Giersch, L., Audrain, M., Parker, S. & Cartier, N. Adeno-Associated Virus-Based Gene Therapy for CNS Diseases. *Hum. Gene Ther.* **27**, 478–496 (2016).

11. Dodiya, H. B. *et al*. Differential transduction following basal ganglia administration of distinct pseudotyped AAV capsid serotypes in nonhuman primates. *Mol.Ther.* **18**, 579–587 (2010).

12. Castle, M. J., Turunen, H. T., Vandenberghe, L. H. & Wolfe, J. H. Controlling AAV Tropism in the Nervous System with Natural and Engineered Capsids. *Methods Mol. Biol.* **1382**, 133–149 (2016).

13. Burger, C. *et al*. Recombinant AAV viral vectors pseudotyped with viral capsids from serotypes 1, 2, and 5 display differential efficiency and cell tropism after delivery to different regions of the central nervous system. *Mol. Ther.* **10**, 302–317 (2004).

14. Weleber, R. G. *et al*. Results at 2 years after Gene Therapy for RPE-65-Deficient Leber Congenital Amaurosis and Severe Early-Childhood-Onset Retinal Dystrophy. *Opthalmology.* **123**, 1606–20 (2016).

15. Rodrigues, G. A. *et al*. Pharmaceutical Development of AAV-Based Gene Therapy Products for the Eye. *Pharm. Res.* **36**, 29 (2018).

16. Mendell, J. R. *et al*. Single-Dose Gene-Replacement Therapy for Spinal Muscular Atrophy. *N. Engl. J. Med.* **377**, 1713–1722 (2017).

17. Gerstein, H., Lindstrom, M.J. & Burger, C. Gene delivery of Homer1c rescues spatial learning in a rodent model of cognitive aging. *Neurobiol Aging* **34**, 1963-1970 (2013).

18. Rex, C. S. *et al*. Myosin IIb regulates actin dynamics during synaptic plasticity and memory formation. *Neuron* **67**, 603–617 (2010).

19. Dossat, A. M. *et al*. Viral-mediated Zif268 expression in the prefrontal cortex protects against gonadectomy-induced working memory, long-term memory, and social interaction deficits in male rats. *Neuroscience* **340**, 243–257 (2017).

20. Fenno, L., Yizhar, O. & Deisseroth, K. The development and application of optogenetics. *Annu. Rev. Neurosci.* **34**, 389–412 (2011).

21. Urban, D. J. & Roth, B. L. DREADDs (designer receptors exclusively activated by designer drugs): chemogenetic tools with therapeutic utility. *Annu. Rev. Pharmacol. Toxicol.* **55**, 399–417 (2015).

22. Kirik, D. & Bjorklund, A. Modeling CNS neurodegeneration by overexpression of disease-causing proteins using viral vectors. *Trends Neurosci.* **26**, 386–392 (2003).

23. Eslamboli, A. *et al*. Long-term consequences of human alpha-synuclein overexpression in the primate ventral midbrain. *Brain* **130**, 799–815 (2007).

24. Thakur, P. *et al*. Modeling Parkinson's disease pathology by combination of fibril seeds and alpha-synuclein overexpression in the rat brain. *Proc. Natl Acad. Sci. USA* **114**, E8284–E8293 (2017).

25. Franich, N. R. *et al*. AAV vector-mediated RNAi of mutant huntingtin expression is neuroprotective in a novel genetic rat model of Huntington's disease. *Mol. Ther.* **16**, 947–956 (2008).

26. Jang, M., Lee, S. E. & Cho, I. H. Adeno-Associated Viral Vector Serotype DJ-Mediated Overexpression of N171-82Q-Mutant Huntingtin in the Striatum of Juvenile Mice Is a New Model for Huntington's Disease. *Front. Cell Neurosci.* **12**, 157 (2018).

27. Lawlor, P. A. *et al*. Novel rat Alzheimer's disease models based on AAV-mediated gene transfer to selectively increase hippocampal Abeta levels. *Mol. Neurodegener.* **2**, 11 (2007).

28. Ittner, L. M., Klugmann, M. & Ke, Y. D. Adeno-associated virus-based Alzheimer's disease mouse models and potential new therapeutic avenues. *Br. J. Pharmacol.* **176**, 3649–3665 (2019).

29. Fiandaca, M. S., Forsayeth, J. R., Dickinson, P. J. & Bankiewicz, K. S. Image-guided convection-enhanced delivery platform in the treatment of neurological diseases. *Neurotherapeutics.* **5**, 123–127 (2008).

30. Varenika, V. *et al*. Controlled dissemination of AAV vectors in the primate brain. *Prog.Brain Res.* **175**, 163–172 (2009).

31. Richardson, R. M. *et al*. Novel Platform for MRI-Guided Convection-Enhanced Delivery of Therapeutics: Preclinical Validation in Nonhuman Primate Brain. *Stereotact.Funct.Neurosurg.* **89**, 141–151 (2011).

32. Tervo, D. G. *et al*. A Designer AAV Variant Permits Efficient Retrograde Access to Projection Neurons. *Neuron* **92**, 372–382 (2016).

33. Miller, S. M., Marcotulli, D., Shen, A. & Zweifel, L. S. Divergent medial amygdala projections regulate approach-avoidance conflict behavior. *Nat. Neurosci.* **22**, 565–575 (2019).

34. Birdsong, W.T. *et al*. Synapse-specific opioid modulation of thalamo-cortico-striatal circuits. *Elife* **8** (2019).

35. Jackson, J., Karnani, M. M., Zemelman, B. V., Burdakov, D. & Lee, A. K. Inhibitory Control of Prefrontal Cortex by the Claustrum. *Neuron* **99**, 1029–1039 e1024 (2018).

36. Lilley, B. N. *et al*. Genetic access to neurons in the accessory optic system reveals a role for Sema6A in midbrain circuitry mediating motion perception. *J. Comp. Neurol.* **527**, 282–296 (2019).

37. Ren, J. *et al*. Anatomically Defined and Functionally Distinct Dorsal Raphe Serotonin Sub-systems. *Cell* **175**, 472–487 e420 (2018).

38. Balmer, T.S. & Trussell, L.O. Selective targeting of unipolar brush cell subtypes by cerebellar mossy fibers. *Elife* **8** (2019).

39. Vonsattel, J. P. *et al*. Neuropathological classification of Huntington's disease. *J. Neuropathol. Exp. Neurol.* **44**, 559–577 (1985).

40. Novak, M. J. *et al*. Basal ganglia-cortical structural connectivity in Huntington's disease. *Hum. Brain Mapp.* **36**, 1728–1740 (2015).

41. Gargouri, F. *et al*. Longitudinal changes in functional connectivity of cortico-basal ganglia networks in manifests and premanifest huntington's disease. *Hum. Brain Mapp.* **37**, 4112–4128 (2016).

42. Saleem, K.S. & Logothetis, N. *A combined MRI and histology atlas of the rhesus monkey brain in stereotaxic coordinates*, (Academic, London; Burlington, MA, 2007).

43. Szabo, J. Organization of the ascending striatal afferents in monkeys. *J. Comp. Neurol.* **189**, 307–321 (1980).

44. Shipp, S. The functional logic of corticostriatal connections. *Brain Struct. Funct.* **222**, 669–706 (2017).

45. Madan, C. R. Creating 3D visualizations of MRI data: A brief guide. *F1000Res* **4**, 466 (2015).

46. Hadaczek, P. *et al*. Widespread AAV1- and AAV2-mediated transgene expression in the nonhuman primate brain: implications for Huntington's disease. *Mol. Ther. Methods Clin. Dev.* **3**, 16037 (2016).

47. Hadaczek, P. *et al*. Transduction of nonhuman primate brain with adeno-associated virus serotype 1: vector trafficking and immune response. *Hum. Gene Ther.* **20**, 225–237 (2009).

48. Salegio, E. A. *et al*. Axonal transport of adeno-associated viral vectors is serotype-dependent. *Gene Ther.* **20**, 348–352 (2013).

49. Naidoo, J. *et al*. Extensive Transduction and Enhanced Spread of a Modified AAV2 Capsid in the Non-human Primate CNS. *Mol. Ther.* **26**, 2418–2430 (2018).

50. Sullivan, J. A. *et al*. Rationally designed AAV2 and AAVrh8R capsids provide improved transduction in the retina and brain. *Gene Ther.* **25**, 205–219 (2018).

51. Foust, K. D. *et al*. Intravascular AAV9 preferentially targets neonatal neurons and adult astrocytes. *Nat. Biotechnol.* **27**, 59–65 (2009).

52. Deverman, B. E. *et al*. Cre-dependent selection yields AAV variants for widespread gene transfer to the adult brain. *Nat. Biotechnol.* **34**, 204–209 (2016).

53. Liguore, W. A. *et al*. AAV-PHP.B Administration Results in a Differential Pattern of CNS Biodistribution in Non-human Primates Compared with Mice. *Mol. Ther.* **27**, 2018–2037 (2019).

54. Minkova, L. *et al*. Large-scale brain network abnormalities in Huntington's disease revealed by structural covariance. *Hum. Brain Mapp.* **37**, 67–80 (2016).

55. Aggleton, J. P., Pralus, A., Nelson, A. J. & Hornberger, M. Thalamic pathology and memory loss in early Alzheimer's disease: moving the focus from the medial temporal lobe to Papez circuit. *Brain* **139**, 1877–1890 (2016).

56. Bakkour, A., Morris, J. C., Wolk, D. A. & Dickerson, B. C. The effects of aging and Alzheimer's disease on cerebral cortical anatomy: specificity and differential relationships with cognition. *Neuroimage* **76**, 332–344 (2013).

57. Dufour, B. D., Smith, C. A., Clark, R. L., Walker, T. R. & McBride, J. L. Intrajugular vein delivery of AAV9-RNAi prevents neuropathological changes and weight loss in Huntington's disease mice. *Mol. Ther.* **22**, 797–810 (2014).
58. Yushkevich, P. A. *et al.* User-guided 3D active contour segmentation of anatomical structures: significantly improved efficiency and reliability. *NeuroImage* **31**, 1116–1128 (2006).

Acknowledgements

Author contributions

Study design: A.R.W., W.A.L. and J.L.M. Surgical delivery of AAVs: A.R.W., W.A.L., D.B., J.S.D. and J.L.M. Necropsy and tissue collection: A.R.W., W.A.L., D.B., J.S.D. and J.L.M. Histology and microscopy: W.A.L., A.R.W. and J.L.M. Statistical analysis: A.R.W, W.A.L. and J.L.M. Figure preparation: A.R.W, W.A.L. and J.L.M. Manuscript preparation: A.R.W, W.A.L. and J.L.M. All authors reviewed the manuscript.

Competing interests

J.L.M. has previously been a paid consultant for Spark Therapeutics and a key opinion leader for Takeda Pharmaceutical Company. J.L.M. is also currently receiving financial compensation for consulting with investigators at Rush University Medical Center and The University at Albany-SUNY regarding an award funded via the Michael J. Fox Foundation for Parkinson's Research. All other authors have no conflicts to report.

Additional information

Supplementary information is available for this paper at https://doi.org/10.1038/s41598-020-63559-7.

Correspondence and requests for materials should be addressed to J.L.M.

Reprints and permissions information is available at www.nature.com/reprints.

Publisher's note Springer Nature remains neutral with regard to jurisdictional claims in published maps and institutional affiliations.